Pulsed laser deposited tetrahedral amorphous carbon with high sp^3 fractions and low optical bandgaps

Y. Miyajima,[a] S. J. Henley, G. Adamopoulos, V. Stolojan, E. Garcia-Caurel,[b] B. Drévillon,[b] J. M. Shannon, and S. R. P. Silva[a]
Nano-Electronic Centre, Advanced Technology Institute, University of Surrey, Guildford GU2 7XH, United Kingdom

(Received 24 January 2008; accepted 7 February 2009; published online 15 April 2009)

Amorphous carbon films with sp^3 bonded carbon fractions over 70% are deposited by pulsed laser deposition. However, the optical bandgap obtained from optical transmittance and spectroscopic ellipsometry analysis shows the values to be below 1.0 eV. A wide range of measurements such as electron energy loss spectroscopy, visible Raman, spectroscopic ellipsometry, optical transmittance, and electrical characterization are performed to elucidate the bonding configurations that dictate microstructural, optical and electrical properties, and their linkage to band structure changes. It is found that stress-induced electronic localized states play an important role in the physical properties of the films deposited. The optical bandgap is shown not to be a good measure of the electrical bandgap, especially for high electric field conduction in these tetrahedral amorphous carbon films.
 [DOI: 10.1063/1.3095667]

I. INTRODUCTION

The possibility of high speed electronic devices using only amorphous carbon (*a*-C) with different fractions of sp^3 bonded carbon layers deposited by pulsed laser deposition (PLD) was reported[1] after many detailed studies.[2–4] The merit of PLD is that it is possible to tune the properties of the films, such as the sp^3 fraction (up to 80%–85%),[5] by changing the laser fluence and the pressure of gas in the chamber. To understand the growth mechanism, the dynamics of a confined carbon plume ablated using a laser from a graphite target was studied using optical emission spectroscopy and ultrafast charge-coupled device imaging.[6] Amorphous carbon films deposited using PLD have been studied using electron energy loss spectroscopy (EELS) to provide information about their sp^2 fraction and their density[7] with the degree of sp^2 clustering obtained from Raman spectroscopy.[8] The concentration and the chemical bonding in the films based on x-ray photoelectron spectroscopy have also been reported.[9] The optical properties were studied using optical transmittance to give the optical bandgaps, and ellipsometry was used to obtain the refractive index. Electrical properties have been measured based on either sandwich or coplanar structures.[10,11]

Lately, a Tauc–Lorentz (TL) model for spectroscopic ellipsometer was developed and applied to *a*-C.[12] It can provide interpretation of the imaginary part of the dielectric constant which is related to the electron transitions between the valence and the conduction bands, i.e., the electronic joint density of states (JDOS) between the occupied valence band and the empty conduction band. Therefore, it is possible to compare the electronic band structure with the data on the position, strength, and broadening of the transition peak and the Tauc optical bandgap, which are extracted from the JDOS between the valence and the conduction band. However, there are few reports that connect the microstructural, optical, and electrical properties via the band structure. Typically, Tauc (E_o) and E_{04} optical bandgaps are measured in order to determine the optical bandgap (E_{opt}) corresponding to the electron transition from π to π^* bands.[13,14] However, when the electrical characterization is discussed, the size of the electrical bandgap (E_g) associated with the extended states in the σ and σ^* bands is important.[14–16] Here, we show that particularly under high electric field conditions, the optical bandgap is a poor measure of the electrical gap, especially when stress is present. It is important to understand the relationship between these properties in order to visualize a broader picture. The electronic density of states (DOS) is influenced by the local and global stress present in the microstructure of the *a*-C films, which in turn influences the physical optoelectronic and mechanical properties of the material. With a good knowledge on these relationships, it may be possible to prepare *a*-C suitable as an electronic semiconductor material.

II. EXPERIMENTAL DETAILS

A. Film deposition

a-C films were deposited using PLD on *c*-Si, mica, and quartz substrates in vacuum at a base pressure of $\sim 10^{-6}$ Torr, evacuated using a turbo molecular pump and backed by a mechanical pump. Quartz and *c*-Si substrates were cleaned using a series of organic solvents then rinsed with de-ionized (DI) water and dried using N_2 gas. The deposition on mica was carried out immediately after cleaving.

A KrF Lambda Physik excimer laser (LPX 210i) operating at 248 nm with 25 ns full width at half maximum (FWHM) pulse duration was used as the UV pulsed laser

[a]Electronic addresses: y.miyajima@surrey.ac.uk and s.silva@surrey.ac.uk.
[b]Laboratoire de Physique des Interfaces et des Couches Minces, UMR 7647 CNRS, Ecole Polytechnique, 91128 Palaiseau Cedex, France.

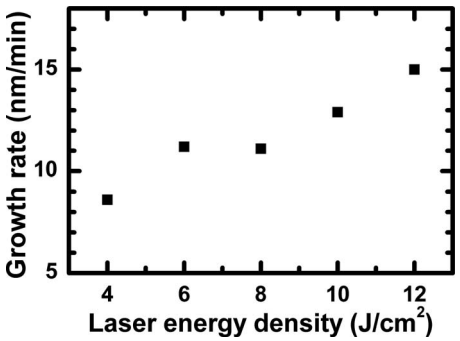

FIG. 1. The growth rate of *a*-C films deposited using different laser fluences.

source for PLD. The laser was incident through a quartz window and was focused onto the surface of a pyrolytic graphite target (Kurt. J. Lesker, 99.99% pure) with 10 cm diameter, which was rotated during deposition to avoid ablation on the same spot. The surface of the target was cleaned using laser ablation with the laser fluence of 4 J/cm^2 before depositions. The repetition rate was fixed at 10 Hz for all depositions. The laser fluence was varied between 4 and 12 J/cm^2. Growth rates were deduced using an atomic force microscopy by measuring the height of a step created by a mask. The results are shown in Fig. 1.

B. Electron energy loss spectroscopy

The sp^2 content of *a*-C films was evaluated using EELS.[17–20] The sp^3 hybridized state forms bonding and antibonding σ and σ^* states, whereas the sp^2 hybridized state creates both σ and σ^* and π and π^* states. Therefore, the sp^2 fraction can be obtained from EELS using the peak corresponding to a transition from occupied 1*s* core electronic states to empty π^* states in the carbon *K* edge spectra. This carbon *K* edge is also the JDOS but between 1*s* core electronic state and the conduction band. Here, the 1*s* core electronic states can be treated as delta function; thus, this carbon *K* edge spectra are effectively the shape of the unoccupied conduction band. The area of the peak was modeled with a Gaussian and normalized to the area under the spectrum from 283 to 294 eV and also to the normalized area of the π^* peak of graphite as the standard of 100% sp^2 bonded carbon.[21] The density of the film can be obtained from the plasmon peak in the low loss energy spectra, assuming that there are four valence electrons per carbon atom.[20–23]

Two transmission electron microscopy (TEM) systems were used for the EELS measurements: a CM200 Philips Supertwin TEM (LaB_6 filament, Gatan Imaging Filter GIF2000 spectrometer) and a Hitachi STEM HD2300A (Schottky field emission gun, Gatan Enfina spectrometer), both operating at 200 kV. The *a*-C samples with a thickness between 30 and 70 nm were immersed in DI water and floated off from mica substrates and then placed on copper TEM grids. As the sp^2 fraction can be obtained using the EELS carbon *K* edge, the corresponding sp^3 fraction can be determined by simple subtraction assuming that only sp^2 and

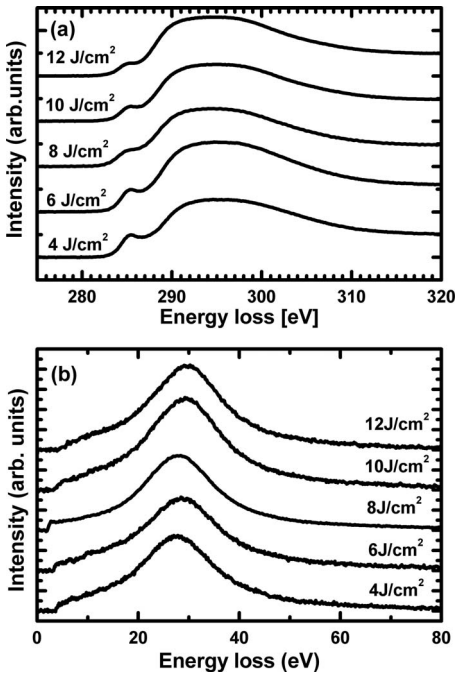

FIG. 2. EELS (a) carbon *K* edge and (b) low loss spectra for different laser fluences.

sp^3 bond hybridizations are present in the sample. Due to the absence of hydrogen it is unlikely that the films contain many *sp* bonds.

The *K* edge and the low loss spectra are shown in Fig. 2 and the sp^3 fraction and the density of the films evaluated from these spectra are shown in Fig. 3.

C. Raman spectroscopy

Visible Raman spectroscopy using 514.5 nm excitation (Renishaw Ramanscope) was used to obtain the microstructural information, especially sp^2 clustering.[24–27] All the *a*-C films show similar Raman spectra consisting of only the *G* peak around 1580 cm^{-1} and almost no *D* peak around 1350 cm^{-1}. The second order TO peak of the Si substrate can be observed at around 960 cm^{-1}, as shown in Fig. 4. The *G* peak is attributed to the stretching mode of all sp^2 carbon and the *D* peak is attributed to the breathing motion of sp^2-aromatic rings, which are activated in disordered carbon when the graphene network is distorted.

Typically, the Raman spectral data were fitted by Briet–Wigner–Fano (BWF)[26,28] shape for the *G* peak and a Lorentzian for the *D* peak.[25] In this study, the Raman spectra of the *a*-C films were fitted with only a BWF line shape as the sp^3 fraction of the film is quite high (over 75%; see Fig. 3) and a clear *D* peak cannot be observed (see Fig. 4).The BWF line shape is described using the equation shown below.

$$I(\omega) = \frac{I_0[1 + 2(\omega - \omega_0)/Q\Gamma]^2}{1 + [2(\omega - \omega_0)/\Gamma]}, \quad (1)$$

where I_0 is the intensity of the peak, ω is the Raman shift, ω_0 is the peak position, Γ is the FWHM of the peak, and Q is the BWF coupling coefficient. The Lorentzian line shape is recovered in the limit of $Q \rightarrow 0$. *G* peak position ω_{max} is evaluated following the equation

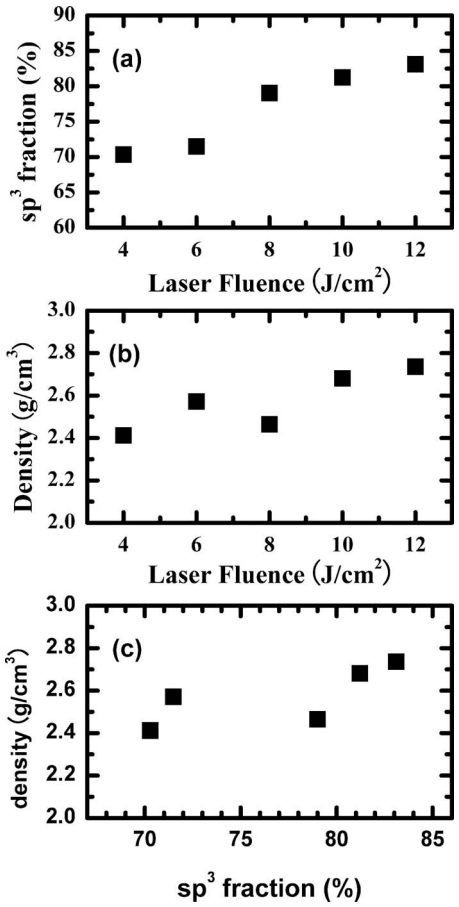

FIG. 3. (a) sp^3 fraction, (b) density of the films with different laser fluences, and (c) density of the films with different sp^3 fractions.

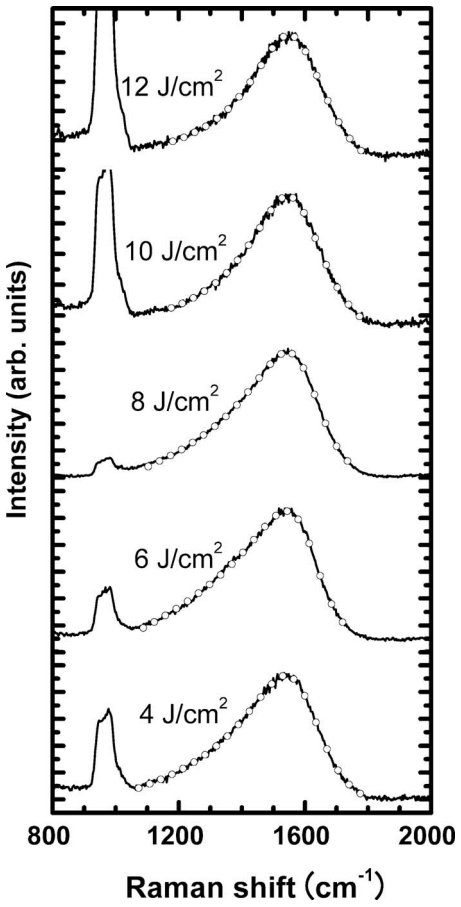

FIG. 4. The visible Raman spectra of *a*-C films deposited using different laser fluences. The dots show BWF curve fitting.

$$\omega_{\max} = \omega_0 + \frac{\Gamma}{2Q}. \tag{2}$$

The fitting parameters, the peak position of the *G* peak, the FWHM of the *G* peak, and the coupling coefficient *Q* are shown in Fig. 5. Here, the peak position of the *G* line is the corrected position [$\omega_{\max}$ (Ref. 25)] and when $1/Q$ becomes zero, the shape of the BWF line shape recovers to the Lorentzian shape.

D. Spectroscopic ellipsometry

The *a*-C films were studied with *ex situ* UV visible spectroscopic ellipsometry (SE) in the range of photon energies from 1.5 to 5 eV using a UVISEL system from Jobin Yvon. For the analysis, a TL analytical expression for the dielectric function[12] was assumed. The SE provides the complex refractive index and allows the extraction of the Tauc optical bandgap (E_o) and the energy at which the optical absorption is 10^4 cm^{-1} (E_{04}). Four parameters for the TL model (A, C, E_o, and E_e) are sufficient to describe the optical functions of the thin film to the accuracy of the ellipsometer.

Jellison and Modine[12] developed this model using the Tauc JDOS and the Lorentz oscillator. The imaginary part ε_i of the dielectric function is given by the product of the imaginary part of Tauc's dielectric function with that of Lorentz. In the parabolic band approximation, Tauc's dielectric function describes interband transitions above the band edge. The new expression for ε_i is described by

$$\varepsilon_i(h\nu) = \left\{ \frac{AE_eC(h\nu - E_o)^2}{((h\nu)^2 - E_e^2)^2 + C^2(h\nu)^2} \times \frac{1}{(h\nu)} \right\} \quad \text{for } h\nu > E_o, \tag{3}$$

$$\varepsilon_i(h\nu) = 0 \quad \text{for } h\nu \le E_o, \tag{4}$$

where A, the optical bandgap E_0, C, and the peak transition energy E_e are fitting parameters. In a single Lorentzian transition, A and C take the significance of the height and FWHM of the transition peak. The fitting model is only valid in the measurement range of SE between 1.5 and 5 eV.

As the carbon *K* edge in EELS is a measure of the empty states in the conduction band, we could deconvolute it from the "pure" Lorentzian JDOS obtained using SE to obtain the valence band DOS (strictly speaking, the C *K* edge is the convolution of 1*s* states with empty 2*p* states, but 1*s* is effectively a delta function compared to 2*p*). This process is currently being investigated as it gets complicated by excitonic effects as well as the effect of the transition decay time.

The real part ε_r of the dielectric function is derived from the expression of ε_i using the Kramers–Kronig integration with new parameter $\varepsilon_{\inf}$.

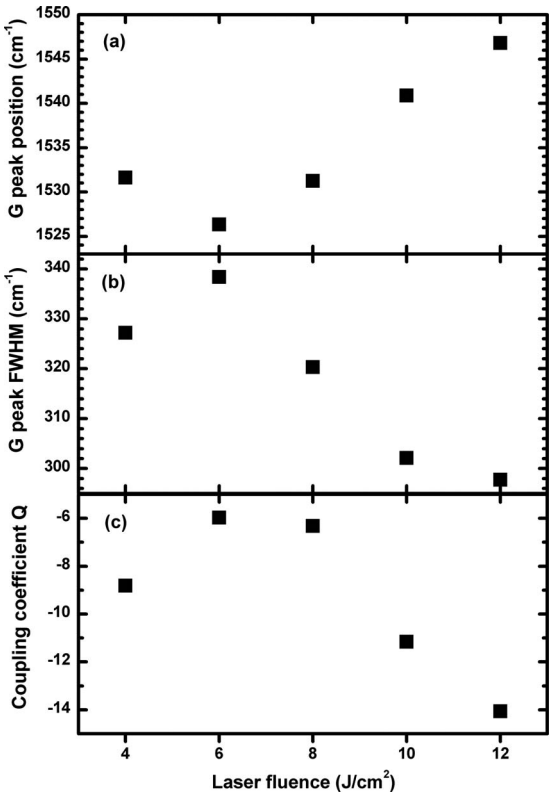

FIG. 5. (a) G peak position, (b) G peak FWHM, and (c) coupling coefficient Q for the visible Raman spectra of a-C films with BWF line shape fitting.

The TL expression is consistent with known physical phenomena within the limitations of the model. At large $h\nu$, the $\varepsilon_i(h\nu)$ of the TL model tends to zero. This is consistent with the observed behavior in the x-ray and γ-ray regimes, where it is known that the absorption coefficient is very small. Furthermore, $\varepsilon_i(h\nu)=0$ below E_o. Mechanisms that give a nonzero value of $\varepsilon_i(h\nu)$ below the bandgap are explicitly ignored in the TL model such as Urbach tail absorption and vibrational absorption in the infrared.[12] Finally, the TL expression is Kramers–Kronig consistent in that $\varepsilon_r(h\nu)$ is determined by Kramers–Kronig integration. The dispersion of the refractive index $n(h\nu)$ and the extinction coefficient $k(h\nu)$ are evaluated from $\varepsilon_r(h\nu)$ and $\varepsilon_i(h\nu)$. It should be noted that the a-C film was fitted using the above models with void due to the inhomogeneity of the film.

Figures 6 and 7 show the fitted parameters of the TL model as well as the refractive index (n) and the extinction coefficient (k) dispersions, respectively. The refractive index at 2 eV, which is the energy that is normally used for monochromatic light source ellipsometry, is shown in Fig. 11.

E. UV-visible-NIR optical transmittance

A Varian Cary 500, UV-visible-NIR spectrometer was used in dual beam mode for the optical transmittance between 190 and 3000 nm (6.5–0.4 eV). Amorphous carbon films with a thickness of around 30 nm on quartz substrates were used. The transmittance was converted to the absorbance coefficient $\alpha[\text{cm}^{-1}]$ to get the optical bandgap E_{04} that corresponds to the photon energy at the absorption coefficient of 10^4 cm^{-1}. The Tauc optical bandgap was also evaluated using a Tauc plot of $(\alpha h\nu)^{1/2}$ versus photon energy $(h\nu)$ (Ref. 29) and the procedure can be found elsewhere.[30]

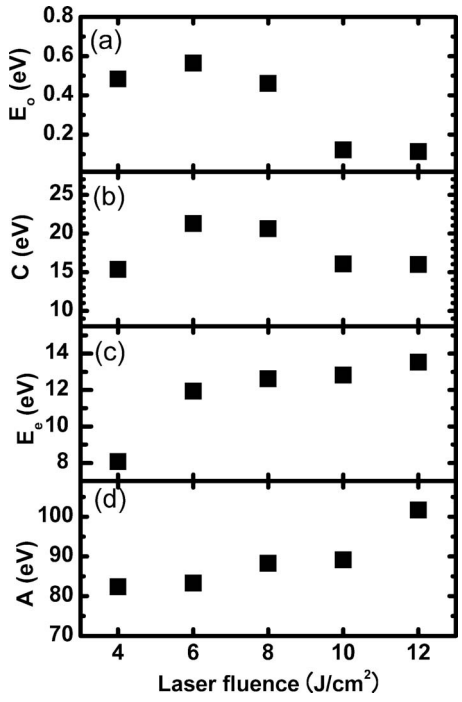

FIG. 6. The parameters of SE obtained from the TL model: (a) Tauc optical bandgap E_o, (b) the broadening factor C, (c) the transition peak central energy E_e, and (d) the strength of the transition peak A.

The optical bandgap (E_{04} evaluated using UV-visible-NIR optical transmittance and Tauc gap evaluated using both UV-visible-NIR optical transmittance and SE) is shown in Fig. 11(a).

F. Electrical characterization

I-V measurements were made on sandwich structures. Highly doped c-Si wafers were used as a substrate for the

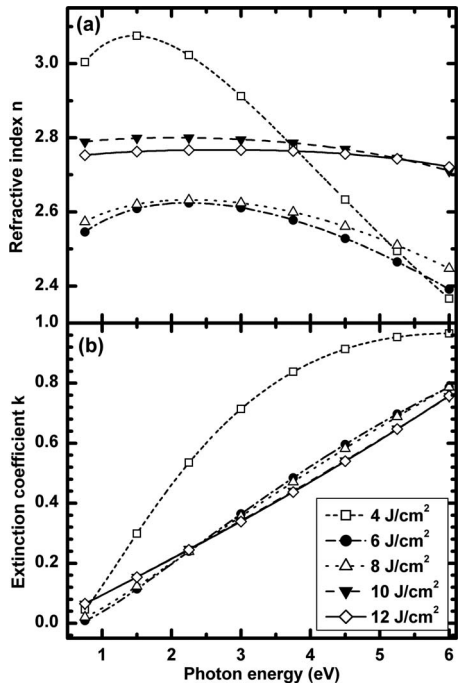

FIG. 7. n and k dispersions for different laser fluences.

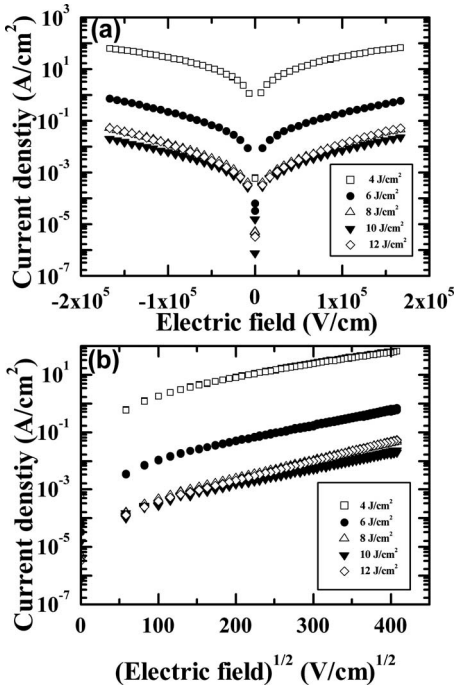

FIG. 8. (a) *J-E* characteristics and (b) PF plot of devices deposited at various laser fluences.

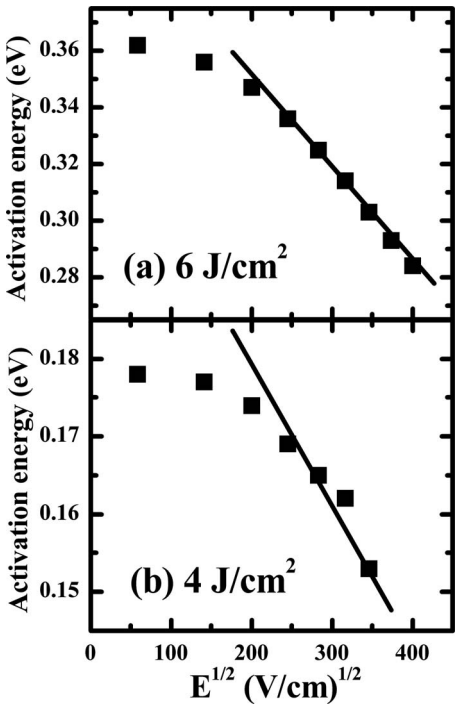

FIG. 9. The activation energy vs the square root of the electric field for *a*-C films deposited with laser fluences of (a) 6 and (b) 4 J/cm^2.

films with 100 nm of dc sputtered aluminum as the back contact. After *a*-C deposition with a thickness of around 30 nm using PLD, a 1.5×10^{-4} mm^2 circular shape top electrode was fabricated using a shadow mask. The top electrode was dc sputtered and composed of 50 nm of Cr coated with 50 nm of Au. Electrical measurements were carried out using a Keithley 236 source meter with a temperature controlled stage that varied between 21 and 80 °C in order to determine the activation energy. The *J-E* characteristics and the square root dependence of the activation energy E_a with electric field are shown in Figs. 8 and 9, respectively.

III. RESULTS AND DISCUSSION

The growth rate of the film increases with increasing laser fluence, as shown in Fig. 1, and is similar to reports published elsewhere.[31] The higher fluence laser ablates more atoms/ions with higher speed from the graphite to the substrate. Henley *et al.*[6] showed that in vacuum, the ablated carbon forms a plume with a speed that reaches 8 km/s, 400 ns after the laser ablation with a laser fluence of 10 J/cm^2. At the pressure range in this study ($<10^{-5}$ Torr), the molecules inside the chamber should not affect the film properties significantly as the mean free path in the vacuum is much longer (>5 m) than the target-substrate distance (6 cm).[32] Thus, on average a few collisions between carbon atoms/ions and the gas molecules are expected while the film forming species transports itself between the target and the substrate, and the carbon plume is thought to reach the substrates without significant loss in momentum. Such high momentum of carbon ions and atoms is thought to form sp^3 hybridized carbon atoms on impact with the growing film and gives higher stress through metastable bond formation in the *a*-C films.

The analysis of the change in the EELS carbon *K* edge and the shift in the plasmon peak energy in low loss spectra enable microstructural information to be extracted such as the sp^3 fraction and the density of the film, as shown in Figs. 2 and 3. The gradual increase in the sp^3 fraction and the density of the films with increasing laser fluence is thought to be the consequence of ballistic transport of carbon species from the target to the substrate. A higher speed carbon plume has a higher energy which can form higher fractions of sp^3 bonding and denser films due to impact densification, whether direct or indirect, as observed in dual magnetron sputtering with ion plating.[24] Figure 3(c) shows that the density reaches almost 2.8 g/cm^3 when the sp^3 fraction exceeds 80%.

Raman spectra show almost no *D* peak; therefore the intensity ratio of the *D* and *G* peaks, $I(D)/I(G)$, is almost zero. This indicates that the sp^2 clustering in the film is low, and such films can be classified as tetrahedral amorphous carbon (ta-C), as reported elsewhere.[25] However, the samples deposited with the laser fluence of 6 and 8 J/cm^2 might have a small *D* peak contribution. The results of curve fitting to the Raman spectrum, the change in the growth rate, the sp^3 fraction, and the density of the film show dispersion around these laser fluences. It might suggest microstructural change occurring in this regime just before the sp^3 fraction reaches 80%. After this point it can be thought that the sp^2 clusters are almost completely separated by the sp^3 matrix. In such a structure, internal stress is thought to be high since sp^2 clusters contribute less to compressive stress associated with *a*-C films.

The TL model with SE fitted parameters is shown in Fig. 6. The dielectric constant in the high energy region (ε_{inf}) is an additional fitting parameter that prevents the imaginary

part of the dielectric constant (ε_r) from converging to zero for energies below the bandgap. Four parameters describe the imaginary part of the dielectric function. A (eV) is related to the strength of the absorption peak, whereas C is the damping coefficient linked to the FWHM of the absorption peak. In general, the FWHM of the peak increases with increasing peak strength [Figs. 6(b) and 6(d)]. The energy of the maximum transition probability and the Tauc optical bandgap are described by E_e (eV) and E_o (eV), and E_e is always higher than E_o as expected.

E_o increases up to a fluence of around 6 J/cm^2 and then decreases with subsequently increasing fluence. This follows the major structural change induced by stress in the films having a high sp^3 fraction which are metastable. C seems to be unchanged apart from 6 and 8 J/cm^2. E_e changes rapidly from 4 to 6 J/cm^2 then gradually increases. A increases with increasing laser power.

It should be pointed out that these four parameters describe the imaginary part of the dielectric function which reflects the electronic JDOS between the valence band and the conduction band. The valence band consists of σ and π bands, whereas the empty conduction band consists of σ^* and π^* bands. σ and σ^* bands are attributed to sp^3 hybridized carbon, whereas π and π^* bands are attributed to the sp^2 hybridized carbon. The π and π^* bands are closer to the Fermi level compared with σ and σ^*; therefore, the increase in E_e and A can be attributed to the increase in the sp^3 fraction as measured by EELS. The rapid increase around 6 J/cm^2 may again indicate a structural change. The broadening factor C for 6 and 8 J/cm^2 is higher than the other samples, which could be attributed to the slight sp^2 clustering that can be seen in the Raman spectra. The value of E_o and its change with increasing laser energy are against the general trend of the optical bandgap[3,13] which shows that films with a higher sp^3 fraction have a higher optical bandgap since the contribution of the π and π^* bands becomes smaller.

However, there are some reports on nonhydrogenated amorphous carbon films which have a high sp^3 fraction and a low optical bandgap.[24,33] When Ar assisted sputtering is used to deposit high sp^3 fraction films, there is a peak energy of Ar ions which gives films that are denser and have high stress. There is a stress induced sp^2 to sp^3 transformation over 13 GPa; thus the sp^3 fraction can reach above 60%. The low optical bandgap was attributed to the small sp^2 clusters in the film which were observed by TEM. The origin of the low optical bandgap was attributed to the high stress in the sputtered films and the oriented sp^2 bonding, as recently observed in ta-C films deposited by filtered vacuum cathodic arc . Actually, the stress of the PLD a-C films used in this study, especially at higher laser fluence films is high. This was supported by the fact that films with thickness above ~50 nm tend to delaminate.

A stress value of 5 GPa has now been calculated, which is based on the difference in the residual stress of the film and estimated from the shift in the G-peak position in the Raman spectrum.[34] The value calculated is of the order expected in these metastable thin films and adds further strength to the arguments we have made of the importance of the local atomic arrangements to the macroscopic properties of the film.

The dispersion of n and k depends on the laser fluence, as shown in Fig. 7. These are evaluated from the real and the imaginary parts of dielectric constant. At low photon energy, n decreases from ~3.1 to 2.6 with increasing laser fluences, and the curves then become almost linear before n increases to around 2.8. The dispersion of k is almost the same for all samples apart from 4 J/cm^2. Higher value of k on the film deposited at 4 J/cm^2 can be attributed to the microstructure of the film since it has the highest sp^2 fraction in this study.

The J-E characteristics measured using the sandwich structures are shown in Fig. 8(a). The conduction mechanism was found to be Poole–Frenkel (PF) conduction at high electric fields ($>10^4$ V/cm) as the log of the current density J is proportional to the square root of the electric field, as shown in Fig. 8(b). The J-E characteristics are symmetric despite the contact materials being different (n^{++}Si for the bottom and Cr for the top contacts),[35] which shows that the current is limited by conduction through the bulk of the film.

If the conduction mechanism follows the PF model, the current density (J) for this situation is given by[35,36]

$$J = eN\mu^* E \exp\left[\frac{-(\Phi - (\beta_{\mathrm{PF}}/\gamma)\sqrt{E})}{kT}\right], \tag{5}$$

where

$$\beta_{\mathrm{PF}} = \sqrt{\frac{e^3}{\pi\varepsilon_r\varepsilon_0}}. \tag{6}$$

Here, Φ is the depth of the neutral trapping centers, E is the electric field across the film, N is the density of the trapping canters, μ is the effective mobility, and γ is the coefficient that changes from one to two depending on the concentration of defects and the degree of compensation.[36,37] When $\gamma=1$, this equation is identical to the classical PF equation. The dielectric constant of the film can be determined from the PF coefficient given by Eq. (6). The activation energy (E_a) for the conduction process at a given field can be obtained from Eq. (5) by measuring current density over a range of temperature. The only unknown is then the product of trap concentration and mobility ($N\mu^*$).

It was also shown that the activation energy is proportional to the square root of the electric field at high fields, as shown in Fig. 9, which is a further indication that PF conduction via neutral localized states is the dominant conduction mechanism at high electric fields. From these plots, the depth of the neutral trapping centers was calculated to be 0.21 and 0.42 eV for 4 and 6 J/cm^2 samples, respectively. There is also a possibility that PF-type conduction might go through two or more localized states instead of the edge of the conduction bands.[38]

The dielectric constants were evaluated using the PF plot and compared with the square of n at 2 eV, as shown in Fig. 10(a). There is a remarkably good agreement in view of all the approximations made. The dielectric constant at high frequency and the conductivity at low fields are shown in Figs. 10(b) and 10(c), respectively. The dielectric constant gives

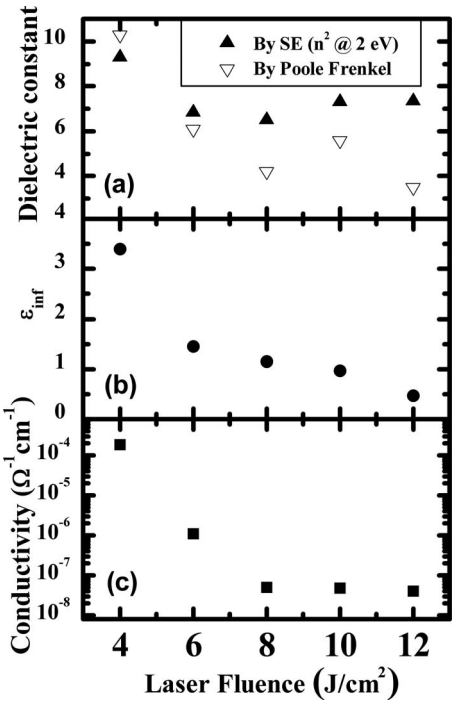

FIG. 10. (a) Dielectric constant evaluated from PF plot and n^2 (at 2 eV) evaluated from SE. (b) The dielectric constant at high energy (x-ray and γ-ray regions) which is used for SE fitting and (c) the conductivity evaluated from low electric fields.

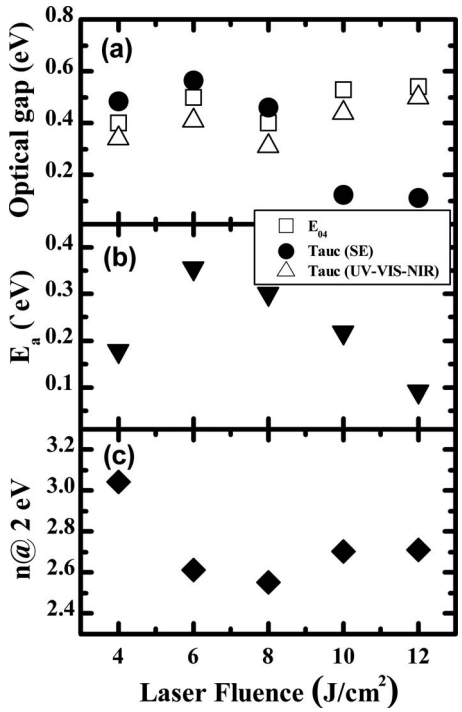

FIG. 11. (a) The optical bandgap (E_{04} and Tauc from UV-visible-NIR and SE), (b) the activation energy measured at low electric fields, and (c) the refractive index n at 2 eV for different laser fluences.

the magnitude of the electrostatic attraction between charged centers and carriers and also between opposite charged carriers (electrons and holes). The increase in the dielectric constant reduces the distance at which a charge carrier becomes free from an oppositely charged center.[39] Thus, there is a correlation between ε_{inf} and the conductivity, as shown in Figs. 10(b) and 10(c). The dielectric constant n was extracted using the TL model for SE which gives a better correlation between n, evaluated from PF plots, compared with a former report that used monochromatic ellipsometry.[35] This is particularly true for the sample deposited at 4 J/cm^2. This sample also shows the highest conductivity; thus the highest sp^2 fraction could affect the conductivity at low fields via conduction through the sp^2 network.

Figure 11(a) shows the optical bandgaps evaluated from UV-visible-NIR and SE. Both the SE and the optical transmittance measurements give an optical bandgap <1 eV even when the sp^3 fraction is more than 70%. In general, higher sp^3 fraction films have higher optical bandgaps since the contribution of σ^* and σ is larger. The different optical bandgap obtained by optical transmittance and SE at high laser fluences could be due to the fact that SE takes into account the reflections of the films, whereas the optical transmittance does not. The other possibility is that these films were very absorbing and a long Urbach tail is present, which is reflected in the low optical bandgap. The Tauc gap from an optical transmittance measurement was obtained from the Tauc plot, whereas the Tauc gap from SE is obtained as a fitting parameter to a range of energies. As SE does not take into account the Urbach tail in the infrared region, when the films have a large contribution from stress induced electronic localized states in the low energy region, SE would probably provide a smaller gap. UV-visible-NIR optical transmittance gives the optical bandgap, but this may have little correlation with the electrical gap, especially for high fields.

The activation energy evaluated at low fields and the refractive index at 2 eV are also shown in Figs. 11(b) and 11(c), respectively. Here, the electric field is less than 10^4 V/cm and the J-E characteristic is linear. As it has already been stated, the conduction mechanism at high fields was confirmed to be PF bulk limited conduction. It means that the conduction band might contribute to the conduction only under high electric fields. The possible conduction mechanism for low electric fields is thought to be dominated by band tail hopping,[40] which occurs via defects in the band tail above the Fermi level. In such a case, the activation energy is an indication of the energy between the defects and the Fermi level. Such defects are thought to be at the bottom of the empty electronic localized π^* band or stress induced electronic localized states close to the Fermi level. Therefore, the very low activation energies at high laser fluence can be explained by a high density of stress and disorder induced defects.

It is important to point out that stress induced electronic states might be attributed to the "weak bonds" formed by π and π^* bonds.[41,42] The deposition condition defines the microstructure of the films such as sp^3 ratio and the internal stress. When the sp^3 ratio and the internal stress are high, small sp^2 clusters are thought to exist, and some of the π and π^* bonds might be the weak bonds. If so, such weak bonds create the electronic localized states in the midgap; consequently the optical bandgap of such a-C films decreases. Such electronic localized states can be thought to contribute to the electrical conduction as defects or neutral defects, and

laser annealing on PLD deposited *a*-C supports this concept.[43] Then, there is a possibility that the PF bulk limited conduction occurs through such electronic localized states or bands in the midgap formed by weak bonds.

IV. CONCLUSION

The microstructural, optical, and electrical properties of pulsed laser deposited *a*-C films containing a high fraction of sp^3 bonds were analyzed using optical and electrical measurements. The TL model for SE gives a better understanding of optical properties than monochromatic ellipsometry with the parameters showing good correlation with measurements such as the electrical EELS and Raman.

These measurements show high sp^3 fractions but a low optical bandgap for PLD ta-C films. This low optical bandgap is attributed to the high sp^3 induced electronic localized states in the gap via stress. The major microstructural change appears to occur when the sp^3 fraction of the film exceeds 80%. In such a region, the optical bandgaps evaluated from UV-visible-NIR and SE are different. This is attributed to the presence of Urbach tail-like stress induced electronic localized states due to the disorder and weak bonds.

The electrical conduction mechanism at low electric fields seems to be dominated by band tail hopping via stress induced electronic localized states close to the Fermi level at the bottom of the localized π^* band. When high electric fields are applied, the conduction band can contribute to the conduction via a PF conduction.

Stress, disorder, and weak bonds are related to laser fluence and the energy of the carbon incident on the substrate. The use of lower laser power and an ambient gas to reduce the energy of the carbon reduces stress but also lowers the sp^3 fraction and therefore the optical bandgap. To fabricate a nanoelectronic device such as resonant tunneling diodes that operate in the high field region improvements to the quality of the material will need to be made.

ACKNOWLEDGMENTS

The authors are grateful to the EPSRC, U.K. for funding this program via a Portfolio Partnership award.

[1]S. Bhattacharyya, S. J. Henley, E. Mendoza, L. Gomez-Rojas, J. Allam, and S. R. P. Silva, Nature Mater. **5**, 19 (2006).
[2]S. R. P. Silva, B. Rafferty, G. A. J. Amaratunga, J. Schwan, D. F. Franceschini, and L. M. Brown, Diamond Relat. Mater. **5**, 401 (1996).
[3]*Amorphous Carbon: State of the Art*, edited by S. R. P. Silva, J. Robertson, W. I. Milne, and G. A. J. Amaratunga (World Scientific, Singapore, 1997).
[4]J. Robertson, Mater. Sci. Eng. R. **37**, 129 (2002).
[5]G. Reisse, S. Weissmantel, and D. Rost, Appl. Phys. A: Mater. Sci. Process. **79**, 1275 (2004).
[6]S. J. Henley, J. D. Carey, S. R. P. Silva, G. M. Fuge, M. N. R. Ashfold, and D. Anglos, Phys. Rev. B **72**, 205413 (2005).
[7]P. Kovarik, E. B. D. Bourdon, and R. H. Prince, Phys. Rev. B **48**, 12123 (1993).
[8]M. P. Siegal, J. C. Barbour, P. N. Provencio, D. R. Tallant, and T. A. Friedmann, Appl. Phys. Lett. **73**, 759 (1998).
[9]R. Haerle, A. Pasquarello, and A. Baldereschi, Comput. Mater. Sci. **22**, 67 (2001).
[10]T. Katsuno, C. Godet, A. S. Loir, and F. Garrelier, J. Non-Cryst. Solids **352**, 1421 (2006).
[11]Q. Z. Xue and X. Zhang, Carbon **43**, 760 (2005).
[12]G. E. Jellison and F. A. Modine, Appl. Phys. Lett. **69**, 371 (1996).
[13]*Properties of Amorphous Carbon*, edited by S. R. P. Silva (INSPEC Publication/IEE, London, 2003).
[14]J. Robertson, Diamond Relat. Mater. **6**, 212 (1997).
[15]S. R. P. Silva and G. A. J. Amaratunga, Thin Solid Films **253**, 146 (1994).
[16]G. A. J. Amaratunga, V. S. Veerasamy, W. I. Milne, C. A. Davis, S. R. P. Silva, and H. S. Mackenzie, Appl. Phys. Lett. **63**, 370 (1993).
[17]S. D. Berger, D. R. Mckenzie, and P. J. Martin, Philos. Mag. Lett. **57**, 285 (1988).
[18]P. J. Fallon, V. S. Veerasamy, C. A. Davis, J. Robertson, G. A. J. Amaratunga, W. I. Milne, and J. Koskinen, Phys. Rev. B **48**, 4777 (1993).
[19]J. Fink, T. Mullerheinzerling, J. Pfluger, A. Bubenzer, P. Koidl, and G. Crecelius, Solid State Commun. **47**, 687 (1983).
[20]S. R. P. Silva and V. Stolojan, Thin Solid Films **488**, 283 (2005).
[21]A. J. Papworth, C. J. Kiely, A. P. Burden, S. R. P. Silva, and G. A. J. Amaratunga, Phys. Rev. B **62**, 12628 (2000).
[22]J. T. Titantah and D. Lamoen, Phys. Rev. B **70**, 075115 (2004).
[23]A. C. Ferrari, A. Libassi, B. K. Tanner, V. Stolojan, J. Yuan, L. M. Brown, S. E. Rodil, B. Kleinsorge, and J. Robertson, Phys. Rev. B **62**, 11089 (2000).
[24]J. Schwan, S. Ulrich, T. Theel, H. Roth, H. Ehrhardt, P. Becker, and S. R. P. Silva, J. Appl. Phys. **82**, 6024 (1997).
[25]A. C. Ferrari and J. Robertson, Phys. Rev. B **61**, 14095 (2000).
[26]S. Prawer, K. W. Nugent, Y. Lifshitz, G. D. Lempert, E. Grossman, J. Kulik, I. Avigal, and R. Kalish, Diamond Relat. Mater. **5**, 433 (1996).
[27]A. C. Ferrari and J. Robertson, Phys. Rev. B **64**, 075414 (2001).
[28]M. Yoshikawa, Material Science Forum **52–53**, 365 (1989).
[29]J. Schwan, S. Ulrich, H. Roth, H. Ehrhardt, S. R. P. Silva, J. Robertson, R. Samlenski, and R. Brenn, J. Appl. Phys. **79**, 1416 (1996).
[30]R. A. Street, *Hydrogenated Amorphous Silicon* (Cambridge University Press, Cambridge, England, 1991).
[31]A. A. Voevodin, S. J. P. Laube, S. D. Walck, J. S. Solomon, M. S. Donley, and J. S. Zabinski, J. Appl. Phys. **78**, 4123 (1995).
[32]A. Chambers, *Mordan Vacuum Physics* (CRC, Boca Raton, FL, 2005).
[33]S. Ulrich, C. Bauer, H. Holleck, H. Leiste, M. Stuber, J. Ye, and J. Schwan, Diamond Relat. Mater. **11**, 1010 (2002).
[34]J. K. Shin, C. S. Lee, K. R. Lee, and K. Y. Eun, Appl. Phys. Lett. **78**, 631 (2001).
[35]Y. Miyajima, J. M. Shannon, S. J. Henley, V. Stolojan, D. C. Cox, and S. R. P. Silva, Thin Solid Films **516**, 257 (2007).
[36]S. P. Lau, J. M. Shannon, and B. J. Sealy, J. Non-Cryst. Solids **227–230**, 533 (1998).
[37]J. G. Simmons, Phys. Rev. **155**, 657 (1967).
[38]C. Ronning, U. Griesmeier, M. Gross, H. C. Hofsass, R. G. Downing, and G. P. Lamaze, Diamond Relat. Mater. **4**, 666 (1995).
[39]B. A. Gregg, S. G. Chen, and R. A. Cormier, Chem. Mater. **16**, 4586 (2004).
[40]G. Lazar, K. Zellama, M. Clin, and C. Godet, Appl. Phys. Lett. **85**, 6176 (2004).
[41]M. Stutzmann, Philos. Mag. B **60**, 531 (1989).
[42]J. Robertson, Philos. Mag. B **76**, 335 (1997).
[43]Y. Miyajima, A. A. D. T. Adikaari, S. J. Henley, J. M. Shannon, and S. R. P. Silva, Appl. Phys. Lett. **92**, 152104 (2008).